https://doi.org/10.5194/egusphere-2025-5647
Preprint. Discussion started: 17 February 2026

Spatiotemporal dynamics of atmospheric CO_2 across China revealed by long-term, high-resolution satellite-derived data

Qingqing He[1, 2, *], Yuan Liu[1], Zizheng Li[1], Tong Ye[1], Jingru Cao[1]

[1] School of Resource and Environmental Engineering, Wuhan University of Technology, Wuhan 430070, China
[2] Department of Atmospheric & Oceanic Sciences, University of California, Los Angeles, Los Angeles, California 90095, United States

Correspondence to: Qingqing He (qqhe@whut.edu.cn)

Abstract: Understanding the spatiotemporal dynamics of atmospheric carbon dioxide (CO_2) is fundamental for advancing climate change research and designing effective mitigation strategies. Yet current analyses are constrained by two key limitations: sparse observations that hinder intra-urban assessment and relatively short monitoring periods that limit long-term consistency. To overcome these challenges, we developed a long-term atmospheric CO_2 hindcast modeling framework that generates daily 1-km column-averaged dry-air mole fraction of CO_2 (XCO_2) across China for 2000–2020. The framework adapts the proven $PM_{2.5}$ hindcast approach to CO_2 estimation by training an Extremely Randomized Trees model on the residuals between OCO-2 observations and CarbonTracker simulations. The model integrates a comprehensive set of physically interpretable predictors—including MAIAC aerosol optical depth (AOD), NO_2, peroxyacetyl nitrate (PAN), meteorological variables, and land-use indicators—linking CO_2 variability to co-emitted tracers and boundary-layer processes. Rigorous evaluation demonstrated high reliability (cross-validation R^2 = 0.94–0.97, RMSE = 0.82–1.29 ppm; independent validation R^2 = 0.82–0.97). The resulting long-term, high-resolution dataset reveals distinct carbon hotspots and their evolution: the North China Plain remained persistently elevated with rapid increases during 2000–2010, while southern China exhibited accelerated growth after 2010. Enhancement analyses identified consistent intra-regional hotspots in southeastern Beijing-Tianjin-Hebei and northern Zhejiang, with emissions declining after 2012 and rebounding after 2018. During the Wuhan COVID-19 lockdown, urban cores showed sharper reductions than suburban areas. Our findings underscore the urgency of sustained, spatially targeted emission reduction efforts in future climate strategies. The proposed XCO_2 hindcast modeling framework and the resulting long-term dataset provide a valuable foundation for advancing carbon-neutrality assessments and guiding climate policy across multiple spatial scales.

1. Introduction

With rapid urbanization and economic growth, anthropogenic activities such as fossil fuel combustion, industrial processes, and land-use changes have significantly increased atmospheric carbon dioxide (CO_2) concentrations (Ma and Ogata, 2024). As the primary driver of global climate change, CO_2 alters the Earth's energy balance, accelerates global warming, and disrupts ecosystems and biodiversity (Kabir et al., 2023). Notably, China recorded a high atmospheric CO_2 concentration of 417 ppm in 2021 at the Mt. Waliguan atmospheric background monitoring site, underscoring the urgent need for effective monitoring and mitigation of its carbon footprint. Due to variations in local carbon sources and sinks, as well as atmospheric transport processes, atmospheric CO_2 exhibits pronounced spatiotemporal variability—particularly in urban areas, where complex anthropogenic activities, land surface characteristics, and micro-environmental conditions play a significant role (Labzovskii et al., 2019; Zhang et al., 2021). Although multiple observation systems, including ground-based networks (TCCON, 2022; WDCGG, 2024), chemical transport models and reanalyses (Andrew and Kenneth, 2023), and satellite-derived column-averaged dry-air mole fraction of CO_2 (XCO_2) datasets (Hamazaki et al., 2004; Crisp et al., 2017), provide valuable information, significant challenges remain in achieving both high spatiotemporal resolution and long-term continuity. Developing a dataset that combines fine spatial detail, long temporal span, and daily temporal resolution is therefore critical for capturing carbon hotspots and their long-term dynamics—thereby advancing climate science, evaluating mitigation effectiveness, and informing sustainable development and carbon neutrality strategies.

Various methods have been developed to fuse satellite-retrieved XCO_2 with ancillary information to improve the spatial and temporal continuity of atmospheric CO_2 estimates. These approaches include geostatistical interpolation techniques such as co-kriging (Bhattacharjee and Chen, 2020), regression models such as multiple linear regression (Guo et al., 2012), and machine-learning frameworks ranging from extremely randomized trees (He et al., 2022b; Li et al., 2022) to deep-learning architectures such as ResNet and U-Net variants (Cui et al., 2024; He et al., 2024; Wu et al., 2024). Using satellite XCO_2 retrievals as the dependent variable, several gap-free datasets have been produced for China at increasingly refined resolutions—for example, 0.1° products for 2015–2020 (Li et al., 2023; Liu et al., 2024) and 0.25° reconstructions for 2003–2019 (Zhang and Liu, 2023). Among the available satellite sensors, OCO-2 retrievals are most frequently employed because of their relatively fine footprint (~1–2 km) and daily revisit capability (Cui et al., 2024; Li et al., 2022; Wu et al., 2024). Nevertheless, since OCO-2 was launched in 2014 and began providing high-resolution observations in 2015, the temporal coverage of fusion-based XCO_2 datasets that rely exclusively on OCO-2 remains constrained to the recent decade. For instance, our earlier work developed a multi-source fusion model based on OCO-2 XCO_2 to estimate daily 1-km concentrations across China for 2015–2020 (He et al., 2023b). A more recent study (Wang et al., 2025) presented a global 1-km daily XCO_2 reconstruction for 2003–2023 by integrating multiple satellite products and environmental predictors within a deep-learning framework. While this work highlights the growing interest in long-term, high-resolution CO_2 mapping, the scarcity of fine-resolution retrievals prior to the OCO-2 era and the dependence on harmonized coarse-footprint observations underscore the continuing need for physically informed hindcast frameworks that can extend OCO-2–based estimates to earlier years with improved interpretability and physical consistency.

A similar challenge has been addressed in the field of long-term $PM_{2.5}$ estimation. In China, ground-based $PM_{2.5}$ monitoring networks were only established in 2013, yet the need for multi-decadal exposure assessments prompted the development of hindcast frameworks to reconstruct earlier concentrations. Numerous studies have successfully employed statistical and machine-learning models to generate gap-free, high-resolution $PM_{2.5}$ datasets for pre-monitoring years (e.g., 2000–2012) despite the absence of direct observations (Geng et al., 2021; He et al., 2021; He et al., 2023c; Ma et al., 2016). These hindcast frameworks typically involve training models during periods with available measurements (e.g., post-2013) and applying the trained relationships to estimate concentrations for unmonitored years using long-term, consistently available predictors. Validation analyses have shown that such models can reproduce historical $PM_{2.5}$ variability with reasonable fidelity, yielding leave-one-year-out cross-validation R^2 values of approximately 0.40–0.65. Importantly, the success of this approach depends not on replicating long-term trends, but on the relative stability of short-term (e.g., daily) relationships between the target variable and its driving factors over time (Ma et al., 2022). Building on this principle, a comparable hindcast framework can be extended to atmospheric XCO_2 estimation. Although XCO_2 exhibits a monotonic long-term increase due to the global carbon cycle, the short-term coupling between XCO_2 and its meteorological and surface drivers remains physically consistent. Therefore, by leveraging OCO-2–based high-resolution XCO_2

https://doi.org/10.5194/egusphere-2025-5647
Preprint. Discussion started: 17 February 2026

retrievals to train a multi-source fusion model and subsequently applying it to earlier years (e.g., 2000–2014) with continuous predictors, it is possible to produce a physically informed, long-term, high-resolution reconstruction of XCO_2 that overcomes the limited temporal coverage of OCO-2.

What are the levels of atmospheric CO_2 in China, where are the hotspots, and how have they changed over time? To address these critical questions, we developed a long-term, gap-free XCO_2 dataset at a daily scale with a spatial resolution of 0.01° (~1 km). This dataset was produced using a novel long-term XCO_2 hindcast modeling framework, adapted from the $PM_{2.5}$ hindcast modeling approach. The framework employs an Extremely Randomized Trees model to integrate multiple data sources related to atmospheric CO_2 variations and extends predictions back to 2000, covering 15 years prior to the observation period. Additionally, the interpretable machine-learning tool, the SHapley Additive exPlanations (SHAP) local importance method, was utilized to explore the relationship between atmospheric CO_2 and temperature. Our high-resolution XCO_2 dataset and analysis provide essential insights for climate change research and eco-environmental management.

2. Materials and methods

Table S1 summarizes all the multi-source data utilized in this study, including satellite-retrieved and reanalyzed XCO_2, air pollution and meteorological covariates, and geographic high-resolution datasets such as land cover, population density, and elevation. Given that the dependent variable—spatiotemporal high-resolution XCO_2 data from the OCO-2 instrument—is only available for years after 2015, we trained the machine-learning model using samples from 2015 to 2020 and then applied this model to years prior to 2015 to generate the hindcast long-term XCO_2 dataset. The data sources, modeling, and validation processes are described in detail in this section.

2.1 Data source and preprocessing

2.1.1 OCO-2 and CarbonTracker XCO_2 data

In this study, we utilized two distinct XCO_2 data sources to train the machine-learning model: satellite-retrieved XCO_2 observations from OCO-2 and reanalyzed XCO_2 data from CarbonTracker (CT). The OCO-2 satellite delivers a state-of-the-art spaceborne XCO_2 dataset publicly available, featuring a fine spatial resolution of 1.29 km × 2.25 km and an accuracy of approximately 1 ppm. We obtained the OCO-2 Level 2 XCO_2 V10r product (OCO_2_L2_Lite_FP) for the years 2015–2020 from the Goddard Earth Sciences Data and Information Services Center (Michael and Eldering, 2020) and mapped the XCO_2 retrievals to the nearest 0.01° grid cell. To ensure data reliability, we excluded records flagged as unreliable (i.e., xCO_2_quality_flag = 0). The CT XCO_2 data were derived from the CT2022 XCO_2_1330LST product (https://gml.noaa.gov/), which provides global XCO_2 distributions at 13:30 local solar time with a coarser spatial resolution of 3° × 2° (Crisp et al., 2017). To integrate the CT data into our analysis, we resampled it to match the 0.01° grid resolution and calculated the residuals between OCO-2 XCO_2 and CT XCO_2, which were used as the dependent variable for model training.

2.1.2 Air pollution and meteorological covariates

Since nitrogen dioxide is a significant indicator of CO_2 emissions, we utilized hourly reanalysis data from MERRA2-GMI (https://acd-ext.gsfc.nasa.gov/) (0.625° × 0.5°) and EAC4 (https://ads.atmosphere.copernicus.eu/) (0.75° × 0.75°), including

https://doi.org/10.5194/egusphere-2025-5647
Preprint. Discussion started: 17 February 2026

nitrogen dioxide (NO2) and peroxyacetyl nitrate (PAN). Recognizing that aerosol loading often co-varies with atmospheric CO_2 due to shared emission sources and boundary-layer processes (He et al., 2023b), we incorporated daily, high-resolution aerosol optical depth (AOD) fields derived from MODIS Multi-Angle Implementation of Atmospheric Correction (MAIAC) retrievals (He et al., 2023a). To capture the processes of formation, transport, and dispersion of atmospheric CO_2, hourly meteorological fields were sourced from ERA (https://apps.ecmwf.int/) (0.125° × 0.125°) and ERA5 (https://cds.climate.copernicus.eu/) (0.25° × 0.25°) climate reanalysis products. These datasets included radiation, temperature, cloud cover, humidity, evaporation, precipitation, wind speed, total column ozone, and boundary layer height information. Additionally, we employed daily, 1-km Thermal and Reanalysis Integrating Moderate-resolution Spatial-seamless (TRIMS) land surface temperature (LST) data (https://data.tpdc.ac.cn/) to provide fine-scale gradient information for the machine-learning model. All hourly meteorological and air pollution data were averaged or accumulated to obtain daily values, and coarser-resolution data were resampled to a 0.01° × 0.01° grid using bilinear interpolation.

2.1.3 Geographic variables and auxiliary variables

We obtained annual land cover classification data at a spatial resolution of 30 m for the years 2000 to 2020, derived from Landsat imagery using Google Earth Engine (Jie and Huang, 2022), yearly population data with a 1-km spatial resolution were sourced from Landscan (https://landscan.ornl.gov/), and monthly, 1-km vegetation index data were collected from MODIS Terra (https://ladsweb.modaps.eosdis.nasa.gov/). Elevation data at a 30-m resolution were retrieved from the ASTER Global Digital Elevation Model (Version 2) (http://gdex.cr.usgs.gov/). To align with the 1-km grid used in this study, each land cover parameter was aggregated by computing the fraction of each class within the corresponding grid cell, while the 30-m elevation data were interpolated to a 1-km resolution.

We also included latitude and longitude, based on the centroids of the grid cells, to account for spatial variability in atmospheric CO_2. Additionally, Julian day was incorporated as a temporal feature to help the model capture daily variation patterns. These spatial and temporal variables are commonly used in environmental pollutant estimation models to enhance predictive accuracy (Chen et al., 2024c; He et al., 2023b).

2.2 Model development

2.2.1 Feature engineering

The potential predictors described in Section 2.1 (summarized in Table S2) may share overlapping information, potentially leading to increased model complexity and multicollinearity issues during training. To address this and reduce computational costs, we conducted a hierarchical clustering analysis based on Spearman rank-order correlations among the total of 50 explanatory variables. Using a heatmap of the correlated variables (Fig. S1), we identified 24 clusters by applying a threshold of 0.45. Within each cluster, variables were ranked by importance, and all but the top two were removed. This initial screening yielded 37 candidate explanatory variables, from which we further selected 21 top-ranked variables as the final feature set for model development. The final features used in the model are listed in Table 1.

Table 1. Summary of predictors finally used in the fusion model and their corresponding data sources.

Category	Full name	Spatial resolution	Temporal frequency	Data source

Air pollution	Aerosol optical depth	0.01°×0.01°	daily	https://dataverse.harvard.edu/dataverse/atmospheric_data_by_WHUT
	Total column nitrogen dioxide	0.5°×0.625°	hourly	https://acd-ext.gsfc.nasa.gov/
	Total column peroxyacetyl nitrate	0.75°×0.75°	3-hourly	https://ads.atmosphere.copernicus.eu/
Geographical variables	Landcover-Cropland	30m×30m	yearly	https://zenodo.org/records/5816591/
	Landcover-Grassland			
	Digital elevation model	30m×30m	-	http://gdex.cr.usgs.gov/
	Normalized difference vegetation index	1km×1km	monthly	https://ladsweb.modaps.eosdis.nasa.gov/
	Population	30m×30m	yearly	https://landscan.ornl.gov/
Meteorological variables	Land surface temperature	1km×1km	daily	https://cstr.cn/18406.11.Meteoro.tpdc.271252/
	Boundary layer height	0.125°×0.125°	6-hourly	https://apps.ecmwf.int/
	Evaporation	0.25°×0.25°	hourly	https://cds.climate.copernicus.eu/
	Surface pressure			
	TOA incident solar radiation			
	Surface thermal radiation downwards			
	Total column water vapour			
	10-m U wind component			
	10-m V wind component			
	Total column ozone			
Auxiliary variables	Longitude	-	-	Constructed features
	Latitude			
	Day of year			

2.2.2 Model description and training

Using the explanatory variables described above, we developed an extremely randomized tree (ExtraTrees) model to estimate full-coverage daily XCO_2 across China from 2000 to 2020. The ExtraTrees algorithm constructs multiple randomized decision trees and aggregates their outputs to enhance predictive accuracy and robustness. The model was trained on the residuals between OCO-2 and CT XCO_2 as the dependent variable, using samples from 2015 to 2020. To optimize the model's spatiotemporal predictive performance, we used a two-step hyperparameter tuning approach: Bayesian optimization to identify an optimal parameter range, followed by fine-tuning using grid search. The final set of hyperparameters was determined as follows: n_estimators=300, min_samples_split=5, min_samples_leaf=5, max_features=0.7, and max_depth=31. The trained model was then used to generate daily XCO_2 predictions for each grid cell at a 0.01° spatial resolution for the entire study period (2000–2020), assuming that the relationship between XCO_2 and the predictors during 2015–2020 remained consistent throughout the study period (Ma et al., 2022). To interpret the model, we applied SHAP to reveal the localized contributions of individual predictors to the model's output.

2.3 Model validation

2.3.1 Cross-validation methods of overall modeling performance

Based on the 2015-2020 sample dataset, we assessed the predictive performance of the ExtraTrees model using 10-fold cross-validation (CV) across three distinct strategies: sample-based, grid cell-based, and day-based, to evaluate its overall, spatial, and temporal predictive capabilities, respectively. In the sample-based approach, all observations were randomly divided into 10 approximately equal-sized groups. For the grid cell-based CV, the observed grid cells were randomly partitioned into 10 equally sized groups. Similarly, in the day-based CV, the days spanning the entire time period were randomly divided into 10 equal groups. During each of the 10 iterations, nine groups were used as training data to build the model, while the remaining group was used for prediction.

Given the absence of OCO-2 XCO_2 observations before 2015, direct evaluation of the estimates for those years posed a challenge. To address this, we implemented the leave-one-year-out CV method to simulate a hindcast scenario for evaluating the model's performance. This approach involved withholding data from one entire year during each round of model training, mimicking a situation where XCO_2 observations for that year were unavailable. The model was then tested on the withheld year, allowing us to assess its predictive accuracy for pre-2015 estimates. This state-of-the-art evaluation method is widely recognized and has been successfully applied in previous atmospheric modeling studies, such as PM2.5 hindcasting for years without ground-level measurements (He et al., 2023c; He et al., 2023d; Ma et al., 2022). These complementary validation strategies provided a thorough assessment of the model's predictive accuracy across different dimensions of the estimates. Finally, we assessed the model's performance by comparing its estimates with the original OCO-2 retrievals across the ten validation rounds, using R^2, root mean square error (RMSE), and mean absolute error (MAE) as evaluation metrics.

2.3.2 Independent evaluation methods

We also conducted an independent validation using observations from three ground-based carbon monitoring sites to evaluate the reliability of the model estimates. Two sites, Hefei (HF) and Xianghe (XH), are part of the Total Carbon Column Observing Network (TCCON), which uses Fourier Transform Spectrometers to measure total column CO_2 since 2015. Following established protocols (TCCON, 2022), TCCON data were filtered to retain high-quality observations, selecting those with a fractional variation in the solar intensity parameter below 5%. The two sites were used to assess the spatial robustness of the high-resolution estimates. The third site, Mt. Waliguan (WLG), is part of the World Data Centre for Greenhouse Gases (WDCGG) under the World Meteorological Organization. Although the WDCGG data from Mt. Waliguan reflect near-surface CO_2 concentrations rather than satellite-derived columnar XCO_2 values, they were included to evaluate the hindcast estimates for years prior to 2015, focusing on trends in long-term atmospheric CO_2 variations. The model's XCO_2 estimates were compared against ground-based observations at individual grid cells, as well as within larger spatial windows of 1 × 1, 10 × 10, and 100 × 100 grids surrounding each site. To ensure temporal alignment, ground-based observations were averaged over the time window corresponding to satellite overpass times (10:30–16:30) for the HF and XH stations, while for the WLG station, they were averaged over full natural days. Detailed information about the three ground-based CO_2 monitoring sites is provided in Table S3.

2.4 Statistical analysis

2.4.1 Long-term trend

We applied least squares regression (Weatherhead et al., 1998), a widely used method for long-term trend analysis (Hsu et al., 2012; Ma et al., 2016), at the pixel level to assess the long-term XCO_2 trend and its spatial variability. The pixel-based slope was derived from the monthly mean XCO_2 anomaly time series for each pixel, where anomalies were computed by subtracting the corresponding month's average XCO_2 over the entire study period. Given the overall rise in XCO_2 levels from 2000 to 2020, the coefficient of variation, a normalized measure of dispersion defined as the standard deviation divided by the mean, was calculated from the spatial distribution of annual mean XCO_2 values. This approach allows us to track changes in spatial variability over time.

2.4.2 Detecting XCO_2 enhancement

We analyzed the spatiotemporal variations in carbon emissions at pixel level using the widely used XCO_2 enhancement method, which measures deviation relative to a background value (Hakkarainen et al., 2016; Sheng et al., 2021), based on our gap-free XCO_2 estimates. The daily background value was determined as the median XCO_2 over mountainous areas near the target region (elevation >1000 m), which are minimally influenced by human emissions due to their lower population density and reduced industrial and traffic activity compared to adjacent urban areas. For example, in the case of Wuhan, the daily XCO_2 enhancement for each pixel was calculated by subtracting the background value—defined as the median XCO_2 over mountainous areas in western Hubei—from the corresponding XCO_2 estimate, as expressed in Eq. (1). The resulting XCO_2 enhancements were deseasonalized and detrended, where positive values indicate carbon sources, while negative values represent carbon sinks. To assess the impact of the COVID-19 lockdown in Wuhan, we examined XCO_2 enhancement patterns before, during, and after the lockdown period, analyzing how Wuhan's XCO_2 enhancements changed across these phases. Additionally, we applied the same approach to the corresponding period in 2019 as a reference for comparison. The XCO_2 daily median time series over the lockdown period in 2020 and the corresponding period in 2019 is shown in Fig. S2.

$$\Delta \mathrm{XCO_2}\ (i,j,t) = \mathrm{XCO_2}\ (i,j,t) - \mathrm{XCO_2^{bg}}\ (t) \quad (1)$$

where ΔXCO_2 (i, j, t) and XCO_2 (i, j, t) are the XCO_2 enhancement and value at pixel coordinate (i, j) on day t. $XCO_2bg(t)$ is the daily background XCO_2 value on day t. This enhancement method was extended to two major urban agglomerations in China known for elevated XCO_2 levels: the Beijing-Tianjin-Hebei (BTH) region and the Yangtze River Delta (YRD) region. The mountainous areas with elevations above 1000 m used to derive background values were located in western BTH for the BTH region, and in northern Zhejiang and eastern Anhui, adjacent to the YRD, for the YRD region. The corresponding daily background values are presented in Fig. S3.

3. Results and Discussion

3.1 Evaluation results of model performance

3.1.1 Overall modeling performance

Figure 1(a)–(c) shows the results of the overall, spatial, and temporal CV methods applied to the ExtraTrees model, demonstrating strong performance in estimating daily XCO_2 at a 1-km resolution. The R^2 and RMSE values for sample- and grid cell-based CV are both 0.97 and 0.82 ppm, respectively, while the corresponding values for day-based CV are 0.94 and 1.27 ppm. The similarity

https://doi.org/10.5194/egusphere-2025-5647
Preprint. Discussion started: 17 February 2026

in model performance between sample-based and grid cell-based CV can be attributed to the sparse and evenly distributed nature of OCO-2 XCO_2 observations. Across the entire 2015–2020 training dataset, each grid cell contains approximately 1.7 OCO-2 XCO_2 observations on average, with exceeding 65% of grid cells containing only one observation. This distribution results in the training and validation sets for sample-based CV closely resembling those for grid cell-based CV. Regionally, the model 225 demonstrates better predictive performance in North China compared to other regions, as evidenced by higher R^2 values (0.95–0.99 vs. 0.91–0.98) and lower RMSE values (0.61–1.12 ppm vs. 0.70–1.63 ppm) across the three types of validation results (Table S4). Figure 1(h) presents a histogram of prediction errors across different intervals, showing that the bias between OCO-2 observations and model estimates follows a distribution that is approximately normal across XCO_2 intervals.

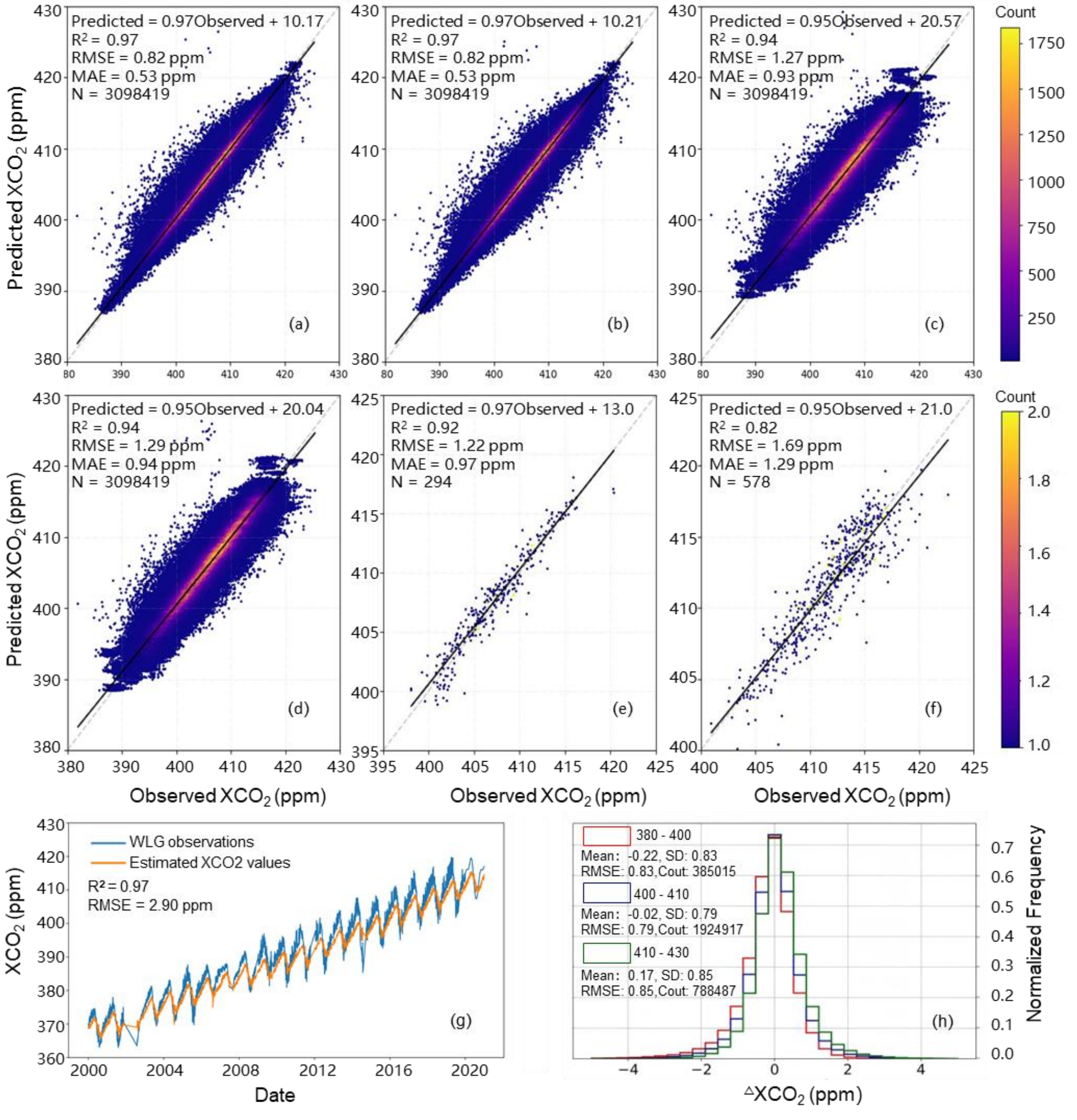

230 **Figure 1. Performance of the long-term XCO_2 hindcast machine-learning model based on CV results and ground-based independent validation. Scatterplots (a)-(d) show (a) sample-based, (b) grid cell–based, and (c) day-based 10-fold CV results, as well as (d) leave-one-year-out CV results derived from the 2015–2020 sample dataset. Independent validation is presented as scatterplots of model-predicted**

XCO_2 versus TCCON observations at the (e) Hefei and (f) Xianghe sites, using a 1 km × 1 km spatial window for 2015–2020. In panels (a)–(f), point colors indicate data density, with colorbars at the upper and middle right for (a)–(d) and the middle right for (e)–(f). Panel (g) compares time series of model-predicted and Mt. Waliguan-observed XCO_2 from 2000 to 2020. Panel (h) shows the distribution of biases between observed and predicted XCO_2 across different intervals.

3.1.2 Validation of pre-2015 estimates

We employed a robust cross-validation approach, the leave-one-year-out CV, to evaluate the model's predictive capability for years without OCO-2 observations. As shown in Fig. 1(d), the hindcast modeling framework effectively predicts long-term XCO_2 values with low uncertainty at the daily level, achieving a validation R^2 of 0.94 and an RMSE of 1.29 ppm. These results are comparable to the accuracy metrics obtained from the day-based CV (Fig. 1(c)), indicating minimal overfitting in the hindcast XCO_2 estimates for years prior to 2015.

We also conducted an independent validation using ground-based observations to assess the reliability of the long-term, high-resolution XCO_2 estimates, particularly for years prior to 2015 when OCO-2 XCO_2 observations were unavailable. The estimated XCO_2 values were well correlated with observations from the two TCCON sites, achieving R^2 values of 0.92 and 0.82 and RMSE values of 1.22 and 1.69 at 1×1 spatial matching window, respectively (Fig. 1e-f, see Table S5 for validation results at 10×10 and 100×100 windows). These results highlight the strong spatial predictive capability of our machine-learning model. At the Mt. Waliguan site, the observed CO_2 concentrations were systematically higher than our estimated XCO_2 values, accompanied by a relatively large RMSE of 2.90 ppm. This discrepancy arises because Mt. Waliguan measures near-surface CO_2 concentrations, whereas both satellite and TCCON sites observe total column CO_2. Therefore, we do not use the RMSE from Mt. Waliguan as an indicator of model accuracy. Nevertheless, the estimated XCO_2 values for 2000–2020 closely reproduced the day-to-day and interannual variations observed at WLG, with an R^2 of 0.97 (Fig. 1g), indicating that our model effectively captures the temporal dynamics of long-term XCO_2 trends.

3.1.3 SHAP importance

We quantified the global and local contributions of input predictors in the high-resolution XCO_2 modeling using average and local SHAP values (Fig.2). The analysis focused on the 2015–2020 samples across three major urban agglomerations—BTH, YRD, and Pearl River Delta (PRD). The overall contribution of each predictor was assessed using the mean absolute SHAP values, which capture the magnitude of influence regardless of direction. Among all predictors, the satellite-derived variable, MAIAC AOD, was a key driver in the prediction of high-resolution daily XCO_2 estimates with the highest average contribution in BTH and ranked among the top four in both YRD and PRD. Although CO_2 itself is not an aerosol component, AOD serves as an indirect indicator of fossil-fuel combustion intensity and atmospheric mixing conditions that influence both particulate and gaseous pollutant accumulation. Regions and periods with elevated AOD typically correspond to strong anthropogenic activity, shallow planetary boundary layers, and enhanced co-emission of carbonaceous species, all of which contribute to localized increases in column CO_2. Including AOD as a predictor thus provides physically interpretable information on emission strength and vertical mixing that complements other meteorological and chemical variables in the model. Therefore, the strong contribution of high-resolution MAIAC AOD, both spatially and temporally, reinforces the reliability of our daily XCO_2 estimates in densely populated regions by improving the representation of fine-scale gradients, particularly in areas lacking direct observations.

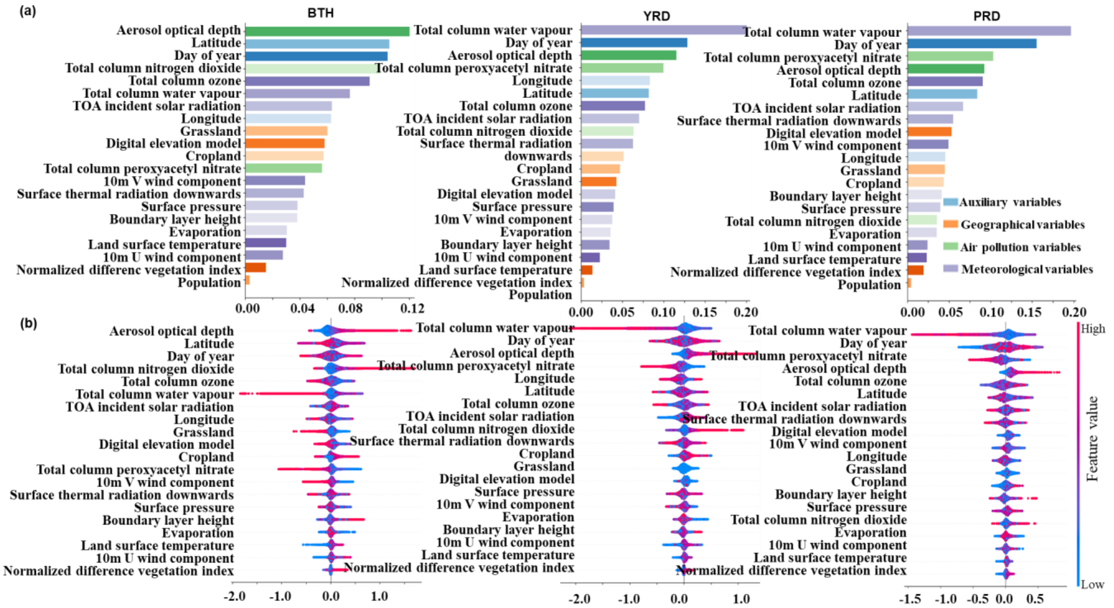

Figure 2. of each predictor on XCO$_2$ levels quantified using the SHAP method over the BTH (left panel), YRD (middle panel), and PRD (right panel) regions: (a) average contribution based on mean absolute SHAP values averaged across grid cell-day samples, with colors indicating predictor categories; (b) distribution of SHAP values for each predictor, with color indicating normalized predictor values.

3.2 Comparisons with other XCO$_2$ datasets and advantages

3.2.1 Improved estimation accuracy

Several previous studies have also derived gap-free XCO$_2$ datasets using machine learning techniques applied to multiple data sources and validated them against ground-based observations. However, their daily estimates generally demonstrated inferior performance compared to ours, with R^2 [RMSE] values of 0.59–0.91 [1.28-2.82 ppm] at the two TCCON sites and R^2 of 0.67 at the WLG site, as shown in Table 2. We also compared the agreements between our estimated XCO$_2$ dataset and global greenhouse gas reanalysis products from CAMS and CT. At the daily level, CAMS and CT XCO$_2$ showed lower consistency with ground-based observations, exhibiting larger biases in both magnitude (RMSE=1.43 – 5.24 ppm) and trends (R^2=0.33 - 0.95) relative to our dataset (R^2=0.82 - 0.97 and RMSE=1.22 – 2.90 ppm; Fig. 1e–f and Table S5). Additionally, we compared our accuracy against another long-term XCO$_2$ dataset derived from the GOSAT instrument using spatiotemporal Kriging interpolation (Chen et al., 2024b), a widely used approach for generating gap-free XCO$_2$ data in earlier studies (Bhattacharjee and Chen, 2020; Chen et al., 2024b). The interpolated XCO$_2$ estimates demonstrated a significantly lower agreement with ground-based measurements than our machine-learning approach, with R^2 values of 0.84, 0.77, and 0.92 for the HF, XH, and WLG stations, respectively. Therefore, with R^2 [RMSE] values of 0.82–0.92 [1.22-1.69 ppm] for the TCCON sites and 0.97 [2.90 ppm] for WLG, our long-term XCO$_2$ estimates achieved better estimation accuracy.

Table 2. Comparison of XCO$_2$ data quality between this study and other datasets.

Datasets	Resolution	Period	XH	HF	WLG

	Spatial	Temporal		R^2	RMSE (ppm)	R^2	RMSE (ppm)	R^2	RMSE (ppm)
Zhang et al., 2022	0.25°	1-month	2003-2019	-	-	-	1.18	-	-
Li et al., 2023	0.1°	1-day	2015-2020	0.86	1.71	0.86	1.71	-	-
Wang et al., 2023	0.25°	1-day	2010-2020	0.73	1.96	0.91	1.28	-	-
Li et al., 2022	0.01°	8-day	2015	-	-	0.59	2.82	-	-
He et al., 2022	0.1°	1-day	2015-2018	-	-	0.76	-	0.67	-
Wu et al., 2024	1km	1-day	2015-2020	0.82	1.56	0.88	1.41	-	-
He et al., 2024	0.25°	1-month	2014-2022	-	1.29	-	0.93	-	-
Cui et al., 2024	0.1°	1-day	2015	-	-	-	1.36	-	-
CAMS (Inness, 2019)	0.75°	1-day	2003-2020	0.33	3.28	0.85	2.10	0.95	2.77
CT (Andrew et al., 2023)	3°×2°	1-day	2000-2020	0.56	2.59	0.90	1.43	0.87	5.24
GOSAT (Chen et al., 2024b)	0.1°	3-day	2010-2019	0.77	2.03	0.84	1.50	0.92	2.90
This study	0.01°	1-day	2000-2020	0.82	1.69	0.92	1.22	0.97	2.90

3.2.2 Enhanced spatiotemporal resolution and coverage

Our modeling output represents the first full-coverage, high spatiotemporal resolution (daily, 1-km) atmospheric CO_2 dataset across China, spanning the longest period to date—from 2000 to 2020. In contrast, previous machine-learning studies have produced daily, 1-km XCO_2 estimates, but their temporal coverage has generally been limited to post-2015 data. This shorter time span constrains the ability to analyze long-term atmospheric CO_2 trends, which are essential for understanding climate change—a fundamentally long-term process.

Figure 3 compares the spatial patterns revealed by our dataset with other widely-used long-term XCO_2 datasets. At the national scale and over the long term, our high-resolution estimates (Fig. 3a) exhibit spatial patterns broadly consistent with CT's coarse-resolution data (Fig. 3b), achieving an average correlation coefficient r of 0.89 (Table S6) over the study period. However, CT's estimates appear notably smoother at both daily and yearly scales, primarily due to their coarser resolution (2° × 3°) nature. By incorporating CT's coarse-resolution data along with other predictors into our fusion modeling process, our outputs capture intra-urban variations with greater accuracy, particularly in eastern China—a region characterized by complex topography, diverse natural landscapes, and intensive human activity (Table 2 and S4). We also compared our dataset with the CAMS global greenhouse gas reanalysis product (Fig. 3c). Similar to CT, the daily XCO_2 data from CAMS share an average correlation of 0.69 with ours but, with a coarser spatial resolution (0.75° × 0.75°), fail to effectively capture intra-city variations. Additionally, our estimates exhibit greater spatial contrast compared to the GOSAT-based interpolated XCO_2 data (Chen et al., 2024b) (Fig. 3d), while still maintaining moderate correlations, with an average r of 0.56. These of accuracy and spatiotemporal patterns underscore the unique

310 advantages of our long-term, high-resolution XCO_2 dataset in capturing day-to-day variations and uncovering detailed spatial gradients in atmospheric CO_2—features often missed by coarse-resolution datasets.

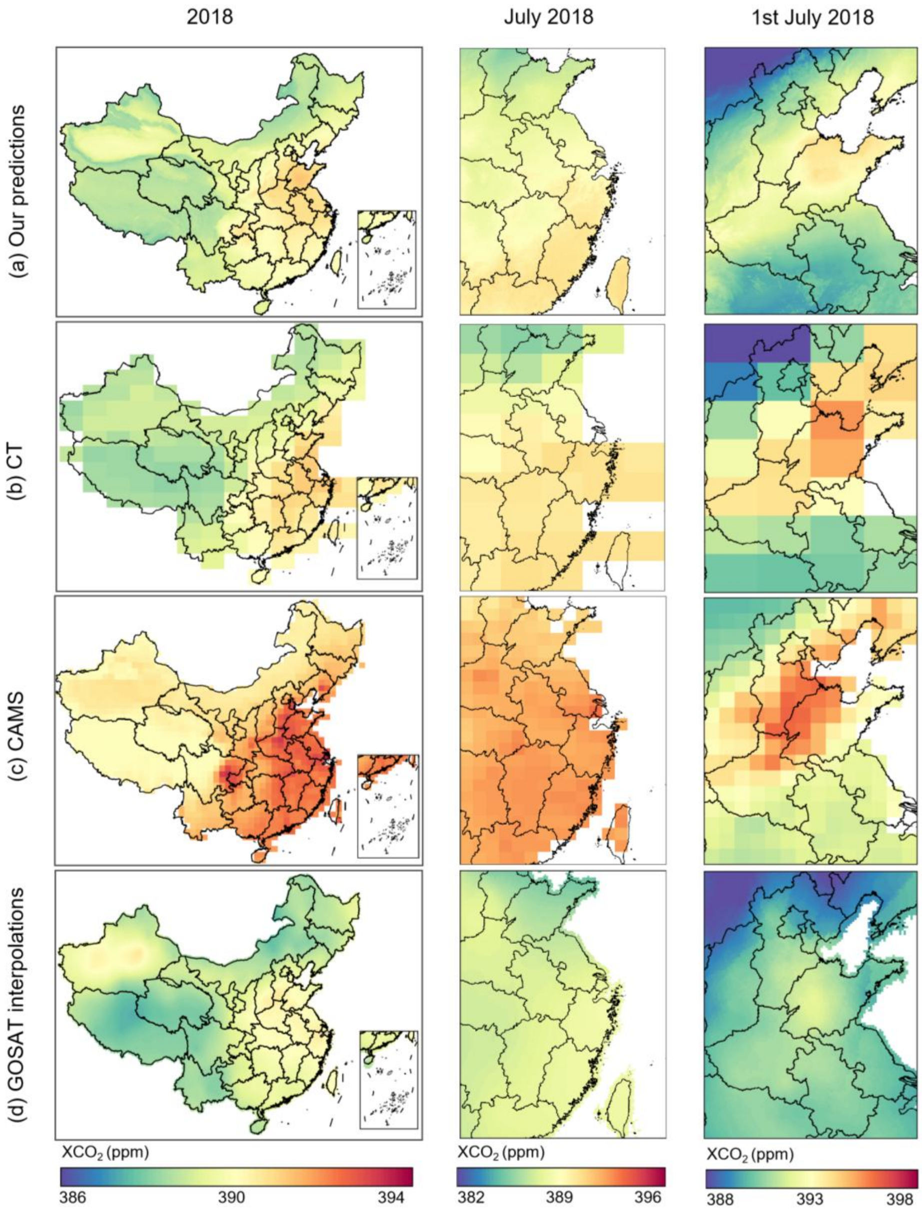

Figure 3. Spatial distribution of XCO_2 values at multiple spatial scales: (a) our predictions (0.01° ×0.01°), (b) CT product (2° × 3°), (c) CAMS product (0.75° × 0.75°), and GOSAT interpolations for a single day (1 July 2018; right column), along with the corresponding monthly (July 2018; middle column) and the annual mean for 2018 (left column). 315

https://doi.org/10.5194/egusphere-2025-5647
Preprint. Discussion started: 17 February 2026

3.3 Spatiotemporal patterns of atmospheric CO_2 in China

3.3.1 Overall spatial pattern and long-term trends

Our modeling outputs effectively capture the long-term, high-resolution spatial patterns of atmospheric CO_2 across China from 2000 to 2020. Utilizing this dataset, this section focuses on a spatiotemporal analysis to uncover the levels of atmospheric CO_2 and variations in hotspot locations over time. On average, the countrywide atmospheric CO_2 level over the past two decades was 390.22 ppm. As shown in Fig. 4a, the highest levels (>391.50 ppm) were concentrated in Shandong and Henan provinces, and gradually decreased across the broader North China Plain (NCP), with XCO_2 ranging between 391.30 ppm and 391.50 ppm. Further reductions in XCO_2 levels were observed moving south, west, and northeast. Overall, eastern China (>390.50 ppm) exhibited higher concentrations compared to the western and northeastern regions, where multiyear mean values were below 390.50 ppm. Within eastern China, the southeastern areas showed relatively lower concentrations, with multiyear mean values below 391 ppm.

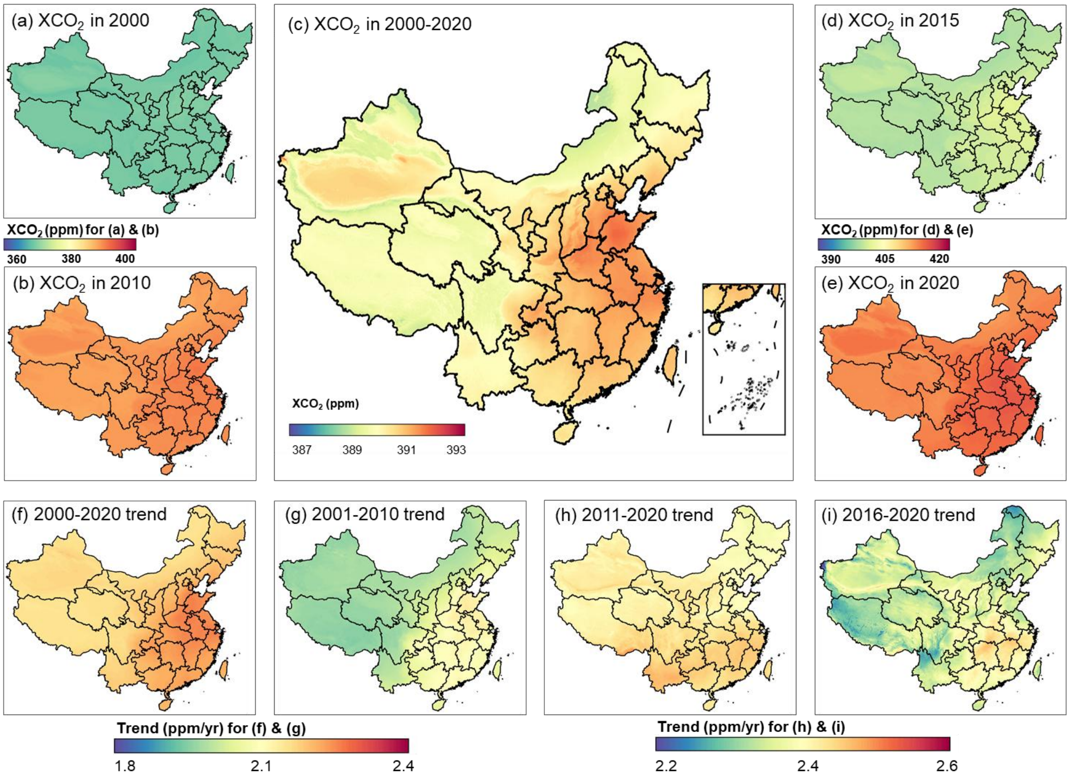

Figure 4. Spatial distributions of atmospheric CO_2 concentrations and their long-term trends across China from 2000 to 2020. The upper panel shows spatial distributions of annual mean XCO_2 for (a) 2000, (b) 2010, (d) 2015, and (e) 2020, as well as (c) the multi-year mean for 2000-2020. The lower panel shows the spatial distributions of statistically significant linear trends ($p<0.05$) for the periods (f) 2000-2020, (g) 2001-2020, (h) 2011-2020, (i) 2016-2020.

National atmospheric CO_2 levels steadily increased from 369.34 ppm in 2000 to 413.12 ppm in 2020, accompanied by growing spatial heterogeneity, as revealed by our pixel-based long-term linear trend analysis (Fig. 4 (f)-(i) and Fig. S4). In 2000, XCO_2 exhibited minimal spatial variation, with a coefficient of variation of just 0.00086 (Fig. S4) and an east–west regional difference of less than 1 ppm. Over the subsequent two decades, however, the east–west difference widened to approximately 3 ppm, and the coefficient of variation rose to 0.00213, driven by spatially heterogeneous increases in CO_2 concentrations. The most pronounced increases were clustered in the NCP region, with slopes exceeding 2.25 ppm/yr ($p < 0.05$), followed by other parts of eastern China, which showed slightly smaller increases (slopes > 2.20 ppm/yr, $p < 0.05$). In contrast, western and northeastern China exhibited relatively smaller trends (slopes < 2.18 ppm/yr, $p < 0.05$). To further explore how trends evolved over time, we divided the study period into two decades: 2001–2010 and 2011–2020. Nationally, the average increasing trend was steeper in the second decade (2.42 ppm/yr) compared to the first (2.01 ppm/yr). However, the spatial distribution of hotspots also shifted. During 2001–2010, the highest increasing trends (slopes > 2.06 ppm/yr, $p < 0.05$) were concentrated in eastern China, particularly in the NCP, where slopes exceeded 2.12 ppm/yr ($p < 0.05$). In contrast, most western areas exhibited trends below 1.98 ppm/yr ($p < 0.05$). In the second decade (2011–2020), although the overall trend strengthened, the NCP showed comparatively smaller increases (slopes of 2.38–2.42 ppm/yr, $p < 0.05$) relative to other regions. Meanwhile, southern China emerged as a hotspot, with trends ranging from 2.44 to 2.48 ppm/yr ($p < 0.05$). Focusing on the most recent five years, the largest increasing trends were observed primarily in central and eastern provinces, such as Hubei, Hunan, Jiangxi, and Anhui. This highlights the spatiotemporal dynamic nature of long-term trends in atmospheric CO_2 levels across China over the past two decades.

The national average atmospheric CO_2 concentrations over the past two decades were 392.27, 388.68, 388.85, and 390.06 ppm in spring, summer, autumn, and winter, respectively (Fig. S5 (a)-(d)). A distinct seasonal pattern emerged, with higher XCO_2 levels in spring compared to summer and autumn across most regions of China. In spring, regions such as Northeast, East, and Central China exhibited seasonal average XCO_2 concentrations exceeding 392 ppm, while in summer and autumn, XCO_2 levels were below 391 ppm across the majority of the country. This observed seasonal variation aligns with the findings of previous studies (He et al., 2022b; He et al., 2023b; Zhang and Liu, 2023). The linear trends of XCO_2 for the four seasons from 2000 to 2020 showed similar spatial patterns, with higher increasing trends concentrated in eastern China (Fig. S5 (e)-(h)). Notably, the trends were particularly pronounced in the NCP and central China during winter, where most areas exhibited slopes exceeding 2.70 ppm/yr (Fig. S5 (h)).

3.3.2 Short-term variability in carbon emission Carbon emission in COVID-19 lockdown

Our daily XCO_2 estimates effectively capture day-to-day variations in atmospheric CO_2, enabling more precise quantification of carbon emission changes during short-term, high-impact events at fine spatial scales. This capability is critical for carbon management and for mitigating the adverse effects of acute emission fluctuations. To illustrate this, we analyzed carbon emission changes associated with the COVID-19 lockdown in Wuhan by comparing XCO_2 enhancements before, during, and after the lockdown period (Fig.5 and Fig. S6). Across all areas of Wuhan and throughout the study period, Wuhan remained a carbon source relative to the background areas, as indicated by consistently positive enhancement values. However, during the lockdown period in 2020, the average XCO_2 enhancement decreased significantly by 43.86% compared to the corresponding period in 2019. In contrast, the post-lockdown period showed similar enhancement levels between the two years, with an average of 0.24 ppm in 2019 vs. 0.23 ppm in 2020. We also observed a substantial ~29.55% decrease in XCO_2 enhancement during the pre-lockdown period, which can be attributed to the earlier timing of the Chinese Lunar New Year holiday in 2020 (January 24–30) compared to 2019 (February 4–10). During the holiday, most industrial operations were suspended or significantly reduced, while daily commuting and freight transport declined sharply, leading to a notable reduction in human-induced carbon emissions. However,

https://doi.org/10.5194/egusphere-2025-5647
Preprint. Discussion started: 17 February 2026

during the first 10 days of both years, the average enhancements remained comparable, with a slight increase in 2020 (1.80 ppm in 2019 vs. 1.84 ppm in 2020), indicating that carbon emissions in the pre-COVID period of 2020 were similar to those in 2019.

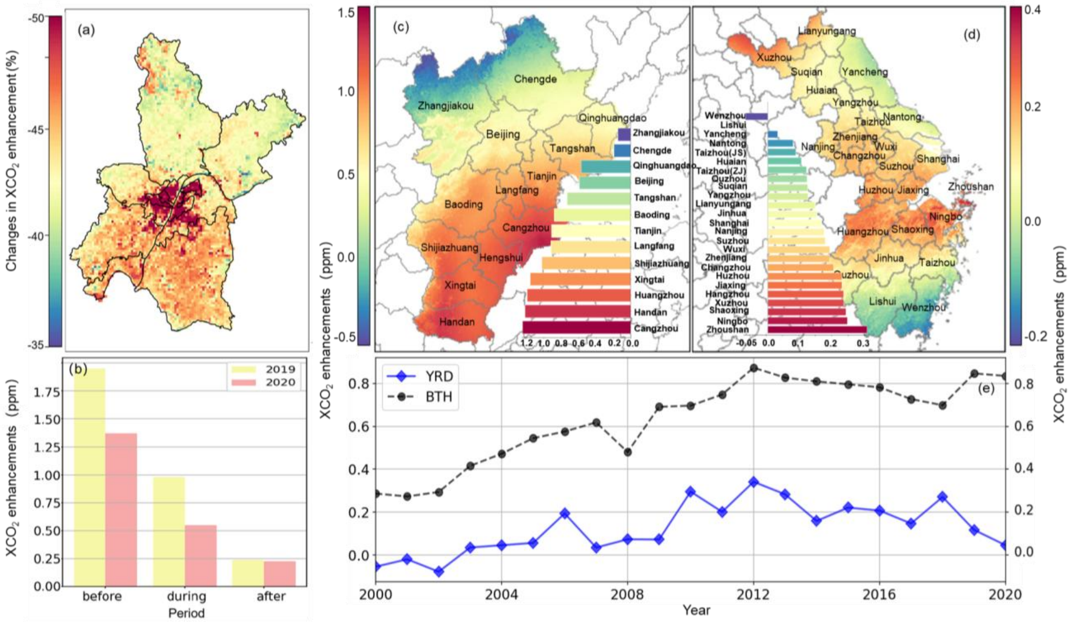

Figure 5. Spatiotemporal distribution of XCO_2 enhancement in selected regions: (a) Spatial distribution of percentage changes in XCO_2 enhancement during the Wuhan lockdown in 2020 relative to the same period in 2019. (b) Comparison of XCO_2 enhancement before (January 1–22), during (January 23–April 7), and after (April 8–May 31) the lockdown in 2020, relative to corresponding periods in 2019. Spatial distributions of multiyear mean XCO_2 enhancement in the (c) BTH and (d) YRD regions over 2000-2020; the inset bar plots present the multiyear, city-level mean XCO_2 enhancement for each region, ranked from lowest to highest. (e) Annual mean time series of XCO_2 enhancement for the BTH (black dotted line) and YRD (blue diamond line) regions.

As shown in Fig. 5d, a striking difference emerged in the spatial patterns of XCO_2 enhancements between the two years. During the lockdown period in 2020, XCO_2 enhancements dropped by over 50% in downtown (central) Wuhan, while reductions were comparatively smaller (40–48%) in suburban areas. The northern suburban regions exhibited the least decline, with most reductions falling below 45%. These spatial differences in XCO_2 enhancements offer valuable insights into urban carbon dynamics and underscore the utility of high-resolution XCO_2 data in understanding anthropogenic emission patterns and informing targeted emission control strategies.

3.3.3 Hotspots of inter- and intra-city carbon enhancement over time

Based on the enhancement analysis using long-term, high-resolution XCO_2 estimates, we examined detailed patterns of carbon emission hotspots across two major urban agglomerations in China (Fig. 5 and S7), both located in the NCP—a region previously identified as exhibiting elevated XCO_2 in the spatiotemporal analysis. Corresponding to the overall XCO_2 variation, the day-to-day evolution of the median background XCO_2 shows a clear long-term increasing trend with pronounced seasonality, averaging 390.27 ± 13.46 ppm for the BTH region and 391.24 ± 13.64 ppm for the YRD region (Fig. S3). Both the BTH and YRD regions

https://doi.org/10.5194/egusphere-2025-5647
Preprint. Discussion started: 17 February 2026

exhibited clear seasonal patterns in XCO_2 enhancements over the past two decades, with consistently higher values in winter and lower values in summer (Fig. S8).

In the BTH region, the long-term average XCO_2 enhancement displays a clear spatial gradient, decreasing from higher positive values (~1.50 ppm) in the southeast to near-zero or slightly negative values (~–0.55 ppm) in the northwest. At the city level, most areas exhibit a similar temporal pattern: a steady increase from 2000 to 2007, followed by a sharp drop in 2008, a rise again through 2012, a decline until 2018, and a rebound in the final two years of the study period. The highest long-term enhancements are observed in Cangzhou (1.20 ppm), a southeastern city bordering Shandong Province, and Handan (1.17 ppm), located in southern Hebei—both adjacent to regions identified as XCO_2 hotspots over the past two decades (Fig. 4). However, the city with the highest annual enhancement varied over time: Shijiazhuang led in the early 2000s, followed by Handan, and then Cangzhou from 2006 onward. In contrast, the lowest enhancements were consistently observed in the northern cities of Zhangjiakou (0.14 ppm) and Chengde (0.18 ppm), which are characterized by higher elevations and lower anthropogenic emissions. In addition to inter-city differences, we also observed substantial intra-city variation. For example, southeastern Cangzhou, bordering the high-emission Shandong Province, showed consistently higher XCO_2 enhancements than its northwestern part. Similarly, western Handan, near the border with Shanxi Province—a region with intensive coal-related activity—exhibited larger enhancements than the eastern part of the city.

In the YRD region, XCO_2 enhancements transitioned from near-zero or slightly negative values in the early 2000s (e.g., –0.05 ppm in 2000 and –0.08 ppm in 2002) to persistently positive values beginning around 2006. The enhancement peaked in 2012 at 0.34 ppm, followed by moderate fluctuations and a general decline after 2013. In 2020, during the COVID-19 pandemic, the average enhancement dropped to 0.046 ppm—the lowest since 2005—indicating a notable reduction. At the city level, long-term enhancement values reveal clear spatial contrasts, with the highest and lowest values generally concentrated in northern and southern Zhejiang, respectively. Ningbo and Shaoxing (both ~0.23 ppm) emerged as persistent enhancement hotspots with the highest long-term averages. In contrast, Lishui (~0.00 ppm) and Wenzhou (–0.07 ppm), both located in southern Zhejiang, recorded near-zero or slightly negative values. Cities in Jiangsu broadly exhibited positive enhancements, with Xuzhou (0.22 ppm)—a northern city bordering Shandong— ranking first within Jiangsu and fourth across the entire YRD region. Meanwhile, eastern coastal cities such as Yancheng (0.03 ppm) and Nantong (0.075 ppm) showed relatively low enhancement values. Similar to the BTH region, significant intra-urban variations were also observed across the YRD. Typically, lower enhancements appeared on the coastal side of Yancheng and Nantong, while the southern parts of Quzhou, Jinhua, and Taizhou—which are adjacent to cities with lower overall enhancements—exhibited lower values than their northern counterparts that border higher-emission areas. In Shanghai, the southwestern districts, known for more intensive industrial activity, showed relatively higher enhancements compared to the Pudong New Area, which is characterized more by commercial, residential, and administrative development than by heavy industry.

4. Discussion

Our XCO_2 fusion modeling framework produced daily 1-km resolution estimates across China for 2000–2020, achieving strong predictive performance ($R^2 = 0.94–0.97$; RMSE = 0.82–1.29 ppm) across four cross-validation schemes. These results surpass existing models—including our previous versions—in terms of accuracy, spatiotemporal resolution, and historical coverage (see

Section 3.2). First, a key innovation of this work is the adoption of the $PM_{2.5}$ hindcast modeling framework, which enabled us to extend high-resolution XCO_2 estimates to the pre-OCO-2 period. While previous global studies, such as Wang et al. (2025), generated long-term global XCO_2 reconstructions by harmonizing multiple coarse-footprint satellite products, our approach anchors the estimation directly to OCO-2 XCO_2 retrievals. The learned relationships between OCO-2 XCO_2 and its predictors are then applied to earlier years (2000–2014), allowing the model to extend both the spatial coverage and temporal span of the OCO-2 record. This represents the first effort to adapt the $PM_{2.5}$ hindcast paradigm to national-scale XCO_2 estimation in China, where data-availability challenges are analogous—$PM_{2.5}$ observations began only after 2013, and OCO-2 data are available from 2015 onward, despite the strong demand for long-term, high-resolution CO_2 fields in climate and environmental studies.

Second, our model improves long-term robustness through a residual-learning strategy that uses the difference between OCO-2 and CT XCO_2 as the dependent variable. This design allows the network to learn fine-scale, process-based deviations from large-scale transport simulations rather than reproducing OCO-2 concentrations directly. Comparative experiments (Table S7) demonstrate that although models trained directly on OCO-2 XCO_2 can achieve similar accuracy during the observed period (R^2 = 0.98, RMSE = 0.75 ppm), they exhibit substantially higher uncertainty when extrapolated to unmonitored years (R^2 = 0.89, RMSE = 1.87 ppm). In contrast, the residual-based model yields more stable hindcast performance, confirming that CT XCO_2 provides a physically consistent baseline for capturing long-term variability. When CT XCO_2 was replaced with other carbon-related predictors, model performance deteriorated notably (temporal and leave-one-year-out R^2 = 0.24–0.53; RMSE = 3.04–4.52 ppm).

Finally, the framework integrates a comprehensive suite of physically interpretable predictors—including MAIAC AOD, NO_2, PAN, meteorological variables, and land-use indicators—that represent key physical and chemical processes influencing column CO_2 concentrations, such as co-emitted combustion tracers, biospheric uptake, and atmospheric transport. In particular, the satellite-derived MAIAC AOD emerged as a dominant driver of high-resolution daily XCO_2 variability, showing high average contributions across the three densely populated urban regions (BTH, YRD, and PRD; Fig. 2). These physically meaningful inputs, combined with the residual-learning design, make the framework data-driven yet physically informed, ensuring consistent performance across both space and time (Fig. 3). Rigorous validation—through leave-one-year-out cross-validation (Fig. 1d), independent comparison with ground-based measurements (Fig. 1e–g), and benchmarking against other long-term datasets (Table S6)—further supports the reliability and physical plausibility of our estimates, including those for the pre-2015 period lacking direct satellite retrievals.

Benefiting from our long-term, high-resolution modeling framework, we investigated the spatial and temporal trends in atmospheric CO_2 levels across China at multiple spatiotemporal scales. Nationally, a distinct east–west gradient was observed in XCO_2 levels, with eastern China, particularly the NCP, exhibiting significantly higher concentrations than the west (Fig. 4), where most areas are characterized by mountainous terrain, deserts, and relatively low human activity (Fig. S8), consistent with previous studies(Lu et al., 2025). While a nationwide increasing trend in XCO_2 was evident over the past two decades, the NCP region experienced steeper increases, highlighting a persistent and concentrated emission hotspot that warrants policy attention.

Zoomed-in enhancement analyses for the BTH and YRD regions—two major urban clusters within the elevated-carbon NCP—revealed persistent carbon emission hotspots at the city level (Fig. 5). In BTH, Cangzhou and Handan showed the highest long-term enhancement values. These cities are located near provincial borders (e.g., Shandong and Shanxi) and are known for intensive industrial activities, including steel production, heavy manufacturing, and coal consumption (Boxer, 2025; Deng and Dong, 2016) . In the YRD region, Zhoushan—an island city—recorded the highest long-term XCO_2 enhancement. As part of the Ningbo–Zhoushan Port, one of the busiest ports in the world, Zhoushan exhibited XCO_2 levels comparable to those of major cities like Ningbo and Jiaxing (Table S8), likely due to its intensive port and shipping activities (Liu et al., 2025). However, the exceptionally high enhancement values may be partially attributable to modeling uncertainties. These uncertainties are likely associated with the coastal and island geographic setting, where challenges such as mixed land–ocean surfaces, lower observation density, and geolocation errors can affect the accuracy of high-resolution model outputs. In contrast, Ningbo and Shaoxing stood out as consistent enhancement hotspots, which can be attributed to their roles as dense industrial and port cities within the Hangzhou Bay economic zone, characterized by high energy consumption and significant transportation-related emissions. In contrast, cities such as Zhangjiakou and Chengde in BTH and Lishui and Wenzhou in YRD exhibited the lowest long-term enhancement values. These areas are relatively less industrialized, more mountainous, and benefit from greater vegetation cover and lower population density, contributing to their lower emissions and possible localized CO_2 uptake. Thanks to the spatial detail provided by our 1-km modeling, we also identified intra-city variations. In both BTH and YRD, lower enhancements were generally found along coastal areas and in city zones bordering regions with lower emissions, while higher values were concentrated in industrial belts and inland districts with intensive energy use and limited ventilation.

Temporally, enhancement trends in both regions (Fig. 5 and S7) generally increased during the first decade and peaked around 2012, followed by a noticeable decline after 2013, aligning with the implementation of China's major air quality initiatives, particularly the Air Pollution Prevention and Control Action Plan launched in 2013 (Shi et al., 2022). Notably, BTH experienced a sharp drop in enhancements in 2008, coinciding with the Beijing Olympics, when strict temporary measures were implemented to reduce industrial output and improve air quality in the capital and surrounding areas (Okuda et al., 2011). The effectiveness of these policies is reflected in the sustained downward trend in enhancements after 2013, supported by large-scale shifts toward cleaner energy, industrial upgrades, and tighter emission controls. However, our results also indicate a rebound in XCO_2 enhancements after 2018, particularly in the BTH region, potentially signaling a resurgence in economic activity and emissions. Although BTH's overall enhancement in 2020 declined relative to 2019 due to the COVID-19 pandemic, the drop was less pronounced than expected and remained higher than in previous years. Based on the 2012–2018 trend, a greater reduction would have been anticipated—suggesting that the lockdown may not have had a lasting suppressive effect on emissions, or that a rapid post-lockdown recovery offset short-term gains. These findings underscore the need for more stringent and sustained carbon control policies to prevent temporary improvements from reversing in the absence of long-term structural changes—particularly in light of China's carbon neutrality goals.

The COVID-19 lockdown in Wuhan further supports our findings, showing a variation pattern consistent with previous Wuhan-specific (Zhang et al., 2023; Cole et al., 2020) that reported abrupt, large decreases (40-60%)) in fossil fuel activity and combustion tracers during the strictest lockdown period. This agreement underscores the capacity of our high-resolution estimates and the enhancement-based approach to capture short-term emission dynamics (Fig. 4; S7). We also observed markedly larger carbon emission reductions in downtown Wuhan than in suburban areas, likely reflecting stricter mobility restrictions and enforcement in the city center, where commercial, service, and transportation activities declined most sharply. Suburban zones likely maintained higher emissions from industry and residential energy use, which were less affected or resumed earlier during reopening. Thus, this case highlights the importance of considering intra-urban emission heterogeneity when designing emission control strategies.

The more substantial reductions in city centers suggest that targeted policies addressing suburban industrial and residential emissions are essential for achieving comprehensive and sustained emission reductions, especially under future low-carbon development goals and emergency response scenarios.

5. Conclusions

In this study, we developed a long-term XCO_2 hindcast modeling framework that generates daily, 1-km atmospheric CO_2 estimates across China for 2000–2020, extending coverage by 15 years prior to the availability of high-resolution OCO-2 observations. The framework adapts the well-established $PM_{2.5}$ hindcast approach to carbon modeling by training an Extremely Randomized Trees model on the residuals between OCO-2 and CT XCO_2. By integrating a comprehensive suite of physically interpretable, long-term predictors, including MAIAC AOD, NO_2, PAN, meteorological variables, and land-use indicators, the model provides physically informed, data-driven reconstructions of atmospheric CO_2 with minimized bias and strong temporal continuity. The resulting high-fidelity, fine-scale dataset enables detailed analyses of atmospheric carbon dynamics, intra- and inter-urban emission hotspots, and long-term regional trends relevant to carbon-neutrality and climate-mitigation strategies. The key findings are summarized as follows:

(1) We successfully extended daily, high-resolution XCO_2 data to a continuous 21-year period (2000–2020), by training a machine-learning model on 2015-2020 samples and applying it hindcast XCO_2 predictions for earlier years. Comparative analyses confirmed that the inclusion of CT data and residual modeling significantly improved the model's robustness, especially for years without satellite observations. SHAP importance analysis indicates that daily, high-resolution MAIAC AOD is a major contributor to modeling XCO_2 over the densely populated regions of BTH, YRD, and PRD, further supporting the representation of high-resolution variations in our XCO_2 estimates, particularly in unmonitored areas with intense human activity.

(2) The NCP emerged as the most persistent long-term XCO_2 hotspot, with Shandong and Henan provinces exhibiting the highest concentrations. While XCO_2 levels rose nationwide throughout the study period, regional trends shifted over time—with the NCP region showing steeper increases during the first decade (2000–2010), and southern China exhibiting faster growth in the second decade (2011–2020), suggesting evolving spatial heterogeneity in emissions.

(3) Enhancement analyses in the BTH and YRD regions, using adjacent mountainous areas as background, revealed distinct emission hotspots in southeastern BTH and northern Zhejiang and southern Jiangsu. Notably, intra-city variation was evident, with lower enhancements near coastal or lower-emission neighboring cities, and higher values in industrial inland areas. Following declines from 2012 to 2018, enhancements rebounded in recent years across both megaregions, raising concerns about a potential resurgence in emissions despite past control efforts.

(4) The case study of Wuhan during the COVID-19 lockdown further demonstrated the model's capacity to capture short-term emission dynamics. XCO_2 enhancements declined citywide, with sharper reductions in downtown areas compared to suburban zones. This underscores the value of high-resolution XCO_2 data for evaluating policy impacts and designing targeted mitigation strategies.

Although this study focuses on China, the framework is readily transferable to other regions or global applications, given its reliance on publicly available predictors and a robust, generalizable methodology. The proposed XCO_2 hindcast framework and dataset thereby offer a valuable resource for advancing carbon-cycle research, evaluating mitigation outcomes, and supporting data-driven climate policy across multiple spatial and temporal scales.

Supplement

Eight tables, and eight figures provide additional information regarding model development and evaluation results of XCO_2 high-resolution modeling.

Author contributions

All authors contributed to the study design, model development, model runs, data analysis, and manuscript writing. QH set up the study, analyzed the data, and wrote the manuscript; YL and ZL developed and implemented the model and revised the manuscript; TY and JC collected and processed the data.

Competing interests

The contact author has declared that none of the authors has any competing interests.

Acknowledgements

The authors are grateful to the editors and anonymous reviewers for their time and constructive feedback, as well as the High-Performance Computing Platform of Wuhan University of Technology for its technical support.

Financial support

This research has been supported by the National Natural Science Foundation of China (Grant NO. 41901324).

References

Andrew, R. J., Kenneth N. S., P.T., and Arlyn, A.: CarbonTracker Documentation CT2022 release, https://gml.noaa.gov/ccgg/carbontracker/CT2022/documentation.php, 2023.

Bhattacharjee, S., and Chen, J.: Prediction of satellite-based column CO_2 concentration by combining emission inventory and LULC information, IEEE Trans. Geosci. Remote Sens., 58, 8285-8300, doi:10.1109/TGRS.2020.2985047, 2020.

Boxer, B.: Shanxi. Encyclopedia Britannica, https://www.britannica.com/place/Shanxi, 2025.

Chen, R., Wang, Z., Zhou, C., Zhang, R., Xie, H., and Li, H.: XCO_2 Data Full-Coverage Mapping in China Based on Random Forest Models, Remote Sens., 17, 48, doi:10.3390/rs17010048, 2024a.

Chen, X., He, Q., Ye, T., Liang, Y., and Li, Y.: Decoding spatiotemporal dynamics in atmospheric CO_2 in Chinese cities: Insights from satellite remote sensing and geographically and temporally weighted regression analysis, Sci. Total Environ., 908, 0048-9697, doi:10.1016/j.scitotenv.2023.167917, 2024b.

Chen, Y., Xie, Y., Dang, X., Huang, B., Wu, C., and Jiao, D.: Spatiotemporal prediction of carbon emissions using a hybrid deep learning model considering temporal and spatial correlations, Environ. Model. Softw., 172, 105937, doi:10.1016/j.envsoft.2023.105937, 2024c.

Cole, M. A., Elliott, R. J., and Liu, B.: The impact of the Wuhan Covid-19 lockdown on air pollution and health: a machine learning and augmented synthetic control approach, Environ. Resource. Econ., 76, 553-580, doi:10.1007/s10640-020-00483-4, 2020.

Crisp, D., Colorado, C.O.D., Eldering, A., Fisher, B., Oyafuso, F., Pane, V., Drouin, B., Toon, G., Laughner, J., Somkuti, P., McGarragh, G., Merrelli, A., Nelson, R., Gunson, M., Frankenberg, C., Osterman, G., Boesch, H., Brown, L., Castano, R., Christi, M., Connor, B., MeDuffie, J., Miller, C, Natrai, V, O'Brien, D, Polonski, I,, Smyth, M., Thompson, D., and Granat, R.: Orbiting carbon observatory (OCO)-2 level 2 full physics algorithm Theoretical Basis Document, https://docserver.gesdisc.eosdis.nasa.gov/public/project/OCO/OCO2_L2_ATBD.pdf, 2023.

Crisp, D., Pollock, H. R., Rosenberg, R., Chapsky, L., Lee, R.A., Oyafuso, F.A., Frankenberg, C., O'Dell, C.W., Bruegge, C.J., and Doran, G.B.: The on-orbit performance of the Orbiting Carbon Observatory-2 (OCO-2) instrument and its radiometrically calibrated products, Atmos. Meas. Tech., 10, 59-81, doi:10.5194/amt-10-59-2017, 2017.

Cui, L., Yang, H., Qiao, Y., Huang, X., Feng, G., Lv, Q.,and Fan, H.: Estimating high spatio-temporal resolution XCO_2 using spatial features deep fusion model, Atmos. Res., 308, 107542, doi:10.1016/j.atmosres.2024.107542, 2024.

Deng, C., and Dong, J. F.: Coal consumption reduction in Shandong province: A dynamic vector autoregression model, Sustainability, 8, 871, doi:10.3390/su8090871, 2016.

Geng, G., Xiao, Q., Liu, S., Liu, X., Cheng, J., Zheng, Y., Xue, T., Tong, D., Zheng, B., Peng, Y., Huang, X., He, K., and Zhang, Q.: Tracking Air Pollution in China: Near Real-Time PM2.5 Retrievals from Multisource Data Fusion, Environ. Sci. Technol., 55, 12106-12115, doi:10.1021/acs.est.1c01863, 2021.

Guo, M., Wang, X., Li, J., Yi, K., Zhong, G., and Tani, H.: Assessment of global carbon dioxide concentration using MODIS and GOSAT data, Sensors, 12, 16368-16389, doi:10.3390/s121216368, 2012.

Hakkarainen, J., Ialongo, I., and Tamminen, J.: Direct space-based observations of anthropogenic CO_2 emission areas from OCO-2. Geophys, Res. Lett., 43, 11400-11406, doi:10.1002/2016GL070885, 2016.

Hamazaki, T., Kuze, A., and Kondo, K.: Sensor system for greenhouse gas observing satellite (GOSAT), In, Optical Science and Technology, the SPIE 49th Annual Meeting, Colorado, United States, 2-6 August 2004, 275-282, doi:10.1117/12.560589, 2004.

He, C., Ji, M., Grieneisen, M.L., and Zhan, Y.: A review of datasets and methods for deriving spatiotemporal distributions of atmospheric CO_2, J. Environ. Manage., 322, 116101, doi:10.1016/j.jenvman.2022.116101, 2022a.

He, C., Ji, M., Li, T., Liu, X., Tang, D., Zhang, S., Luo, Y., Grieneisen, M.L., Zhou, Z., and Zhan, Y.: Deriving Full-Coverage and Fine-Scale XCO_2 Across China Based on OCO-2 Satellite Retrievals and CarbonTracker Output, Geophys. Res. Lett., 49, doi:10.1029/2022GL098435, 2022b.

He, Q., Gao, K., Zhang, L., Song, Y., and Zhang, M.: Satellite-derived 1-km estimates and long-term trends of $PM_{2.5}$ concentrations in China from 2000 to 2018, Environ. Int., 156, 106726, doi:10.1016/j.envint.2021.106726, 2021.

He, Q., Wang, W., Song, Y., Zhang, M., and Huang, B.: Spatiotemporal high-resolution imputation modeling of aerosol optical depth for investigating its full-coverage variation in China from 2003 to 2020, Atmos. Res., 281, 106481, doi:10.1016/j.atmosres.2022.106481, 2023a.

He, Q., Ye, T., Chen, X., Dong, H., Wang, W., Liang, Y., and Li, Y.: Full-coverage mapping high-resolution atmospheric CO_2 concentrations in China from 2015 to 2020: Spatiotemporal variations and coupled trends with particulate pollution, J. Clean. Prod., 428, 139290, doi:10.1016/j.jclepro.2023.139290, 2023b.

He, Q., Ye, T., Wang, W., Luo, M., Song, Y., and Zhang, M.: Spatiotemporally continuous estimates of daily 1-km $PM_{2.5}$ concentrations and their long-term exposure in China from 2000 to 2020, J. Environ. Manage., 342, 118145, doi:10.1016/j.jenvman.2023.118145, 2023c.

He, Q., Ye, T., Zhang, M., and Yuan, Y.: Enhancing the reliability of hindcast modeling for air pollution using history-informed machine learning and satellite remote sensing in China, *Atmos. Environ.*, 312, 119994, doi:10.1016/j.atmosenv.2023.119994, 2023d.

He, Z., Fan, G., Li, X., Gong, F. Y., Liang, M., Gao, L., and Zhou, M.: Spatio-temporal modeling of satellite-observed CO_2 columns in China using deep learning, Int. J. Appl. Earth Obs. Geoinf., 129, 103859, doi:10.1016/j.jag.2024.103859, 2024.

Hsu, N. C., Gautam, R., Sayer, A. M., Bettenhausen, C., Li, C., Jeong, M. J., Tsay, S. C., and Holben, B.N.: Global and regional trends of aerosol optical depth over land and ocean using SeaWiFS measurements from 1997 to 2010, Atmos. Chem. Phys., 12, 8037-8053, doi:10.5194/acp-12-8037-2012, 2012.

Inness, A.: Copernicus Atmosphere Monitoring Service (CAMS) Atmosphere Data Store (ADS), https://ads.atmosphere.copernicus.eu/cdsapp#!/dataset/cams-global-reanalysis-eac4?tab=overview, 2019.

Jie Y., and Huang, X.: The 30 m annual land cover datasets and its dynamics in China from 1990 to 2021, Zenodo [dataset], https://doi.org/10.5281/zenodo.5816591, 2022.

Kabir, M., Habiba, U.E., Khan, W., Shah, A., Rahim, S., De los Rios-Escalante, P. R., Farooqi, Z. U. R., Ali, L., and Shafiq, M.: Climate change due to increasing concentration of carbon dioxide and its impacts on environment in 21st century; a mini review, J. King Saud Univ. Sci., 35, 102693, doi:10.1016/j.jksus.2023.102693, 2023.

Labzovskii, L. D., Jeong, S. J., and Parazoo, N. C.: Working towards confident spaceborne monitoring of carbon emissions from cities using Orbiting Carbon Observatory-2, Remote Sens. Environ., 233, 111359, doi:10.1016/j.rse.2019.111359, 2019.

Li, J., Jia, K., Wei, X., Xia, M., Chen, Z., Yao, Y., Zhang, X., Jiang, H., Yuan, B., and Tao, G.: High-spatiotemporal resolution mapping of spatiotemporally continuous atmospheric CO_2 concentrations over the global continent, Int. J. Appl. Earth Obs. Geoinf., 108, 102743, doi:10.1016/j.jag.2022.102743, 2022.

Li, T., Wu, J., and Wang, T.: Generating daily high-resolution and full-coverage XCO_2 across China from 2015 to 2020 based on OCO-2 and CAMS data, Sci. Total Environ., 893, 164921, doi: 10.1016/j.scitotenv.2023.164921, 2023.

Liu, W., Li, R., Cao, J., Huang, C., Zhang, F., and Zhang, M.: Mapping high-resolution XCO_2 concentrations in China from 2015 to 2020 based on spatiotemporal ensemble learning model, Ecol. Inform., 83, 102806, doi:10.1016/j.ecoinf.2024.102806, 2024.

Liu, W., Xu, B., and Li, J.: Data-Driven Carbon Emission Dynamics Under Ship In-Port Congestion, J. Mar. Sci. Eng., 13, 812, doi:10.3390/jmse13040812, 2025.

Lu, W., Li, X., Li, S., Cheng, T., Guo, Y., and Fang, W.: Effects of Emission Variability on Atmospheric CO_2 Concentrations in Mainland China, Remote Sens., 17, 814, doi:10.3390/rs17050814, 2025.

Ma, B., and Ogata, S.: Impact of Urbanization on Carbon Dioxide Emissions—Evidence from 136 Countries and Regions, Sustainability, 16, 7878, doi:10.3390/su16187878, 2024.

Ma, Z., Dey, S., Christopher, S., Liu, R., Bi, J., Balyan, P., and Liu, Y.: A review of statistical methods used for developing large-scale and long-term $PM_{2.5}$ models from satellite data, Remote Sens. Environ., 269, 112827, doi:10.1016/j.rse.2021.112827, 2022.

Ma, Z., Hu, X., Sayer, A. M., Levy, R., Zhang, Q., Xue, Y., Tong, S., Bi, J., Huang, L., and Liu, Y.: Satellite-Based Spatiotemporal Trends in $PM_{2.5}$ Concentrations: China, 2004-2013, Environ. Health Perspect., 124, 184-192, doi:10.1289/ehp.1409481, 2016.

Michael G., and Eldering, A.: OCO-2 Level 2 bias-corrected XCO_2 and other select fields from the full-physics retrieval aggregated as daily files, Retrospective processing V10r, https://doi.org/10.5067/E4E140XDMPO2, 2020.

Okuda, T., Matsuura, S., Yamaguchi, D., Umemura, T., Hanada, E., Orihara, H., Tanaka, S., He, K., Ma, Y., Cheng, Y., and Liang, L.: The impact of the pollution control measures for the 2008 Beijing Olympic Games on the chemical composition of aerosols, Atmos. Environ., 45, 2789-2794, doi:10.1016/j.atmosenv.2011.01.053, 2011.

Sheng, M., Lei, L., Zeng, Z. C., Rao, W., and Zhang, S.: Detecting the Responses of CO_2 Column Abundances to Anthropogenic Emissions from Satellite Observations of GOSAT and OCO-2, Remote Sens., 13, 3524, doi:10.3390/rs13173524, 2021.

Shi, Q., Zheng, B., Zheng, Y., Tong, D., Liu, Y., Ma, H., Hong, C., Geng, G., Guan, D., and He, K.: Co-benefits of CO_2 emission reduction from China's clean air actions between 2013-2020, Nat Commun., 13, 5061, doi:10.1038/s41467-022-32656-8, 2022.

TCCON: 2020 TCCON Data Release, https://doi.org/10.14291/TCCON.GGG2020, 2022.

Wang, J.: Global Daily 1 Km Gapless Xco2 (2003 – 2023) Derived from Multi-Satellite Observations and a Spatiotemporal Deep Learning Framework, SSRN [preprint], https://ssrn.com/abstract=5234803, 29 April 2025.

WDCGG: Greenhouse Gas Observation Data, https://gaw.kishou.go.jp/, 2024.

Weatherhead, E. C., Reinsel, G. C., Tiao, G. C., Meng, X. L., Choi, D., Cheang, W. K., Keller, T., DeLuisi, J., Wuebbles, D. J., and Kerr, J. B.: Factors affecting the detection of trends: Statistical considerations and applications to environmental data, J. Geophys. Res. Atmos., 103, 17149-17161, doi:10.1029/98JD00995, 1998.

Wu, C., Yang, S., Jiao, D., Chen, Y., Yang, J., and Huang, B.: Estimation of daily XCO_2 at 1 km resolution in China using a spatiotemporal ResNet model, Sci. Total Environ., 954, 176171, doi:10.1016/j.scitotenv.2024.176171, 2024.

Zhang, F., Xuan, X., and Deng, X.: Research progress and prospect on the non-uniform distribution of atmospheric CO_2 concentration and its influence on surface warming, J. Geo-Inf. Sci, 23, 1362-1371, 2021.

Zhang, M., and Liu, G.: Mapping contiguous XCO_2 by machine learning and analyzing the spatio-temporal variation in China from 2003 to 2019, Sci. Total Environ., 858, 159588, doi:10.1016/j.scitotenv.2022.159588, 2023.

Zhang, Q., Boersma, K. F., Zhao, B., Eskes, H., Chen, C., Zheng, H., and Zhang, X.: Quantifying daily NOx and CO_2 emissions from Wuhan using satellite observations from TROPOMI and OCO-2, Atmos. Chem. Phys., 23, 551–563, doi:10.5194/acp-23-551-2023, 2023.